Dielectric Barrier Discharge Plasma Actuators to Mitigate Flow Separation

Maggie Gaskell, Robin Krasinkiewicz, Janet Liu, Noah Miggiani, Charlie Smith, Annie Wu, Haowen Yan, Aidan Woods
Queen's University Aerospace Design Team, Kingston, Ontario, Canada

http://www.imavs.org/

ABSTRACT

The following study investigates dielectric barrier discharge (DBD) plasma actuator enhancement for fixed wing micro air vehicles (MAVs) to mitigate airflow separation and increase the stall angle. Airflow separation optimization allows for controlled flight at low Reynolds numbers for low speeds and high altitudes. The following work implements simulations in computational flow dynamics (CFD) software, including Simscale and Openfoam, to determine the location along the chord length of a NACA0012 airfoil where flow separation occurs for various angles of attack. The resulting data determines that the optimal location for the DBD plasma actuators is with their frontmost edges coincident with the airfoil's leading edge. Transient simulations in OpenFOAM with and without a plasma actuator validate the effectiveness of the actuator location with comparison to non-actuated values from previous studies. The actuator models are developed using momentum sources and Python code was used to graph the data and determine average coefficient and momentum values. Comparisons between the resulting coefficients and those in previous studies determine that at a Reynolds number of 53,000 the actuators consistently increase the lift and decrease the drag coefficients when placed at the leading edge of the airfoil.

1 INTRODUCTION

Flow separation occurs when the boundary layer of air on a wing surface detaches from the wing, causing an increase in parasitic drag and a decrease in lift. Separation often occurs when the wing is subject to adverse pressure gradients or high angles of attack, and in extreme cases can result in a transition from laminar to turbulent flow, leading to aircraft stall. After flow separation occurs, the boundary layer can reattach to the wing further down the chord length, resulting in a separation bubble, in which backflow can occur [1] . Laminar flow, which occurs at low Reynolds numbers (R_e), is more prone to flow separation than turbulent flow. As demonstrated by Equation 1, low R_e flow can occur due to low air density (ρ), low airspeed (v), low chord length (L), or high viscosity (μ). At extremely low R_e, the boundary layer may not reattach after separating, further increasing flight difficulties [2].

$$R_e = \frac{\rho v L}{\mu} \tag{1}$$

Due to the disadvantages of low R_e flow, low speed and high density-altitude flight is often impractical. These limitations are especially prominent in MAVs due to short chord lengths [3] . This narrows the range of altitudes and speeds at which most aircraft can achieve flight, limiting their effectiveness in applications such as flight at the high density-altitudes of Earth's stratosphere, on Mars [3], or low speed flight required in urban environments, such as in urban military combat or search and rescue scenarios [4]. Another limited application is the flight of aircraft used to combat wildfires, due to high density-altitudes caused by the extreme heat.

Flow separation can be mitigated using flat-plate airfoils, as their performance generally does not vary with R_e [2] , or riblets, due to their ability to suppress laminar separation bubbles [5]. However, such methods have notable downsides. Flat-plate airfoils are widely outperformed by thicker airfoils in most applications and thus lack versatility, as they are only useful in low R_e settings [2]. Riblets primarily work to reduce skin-friction drag and thus are not effective on objects with drag forces dominated by pressure drag [6].

An emerging, effective way to mitigate flow separation is the implementation of DBD plasma actuators. They present similar benefits to flat-plate airfoils or riblets, without compromising other aspects of the aircraft's performance. However, actuators introduce other complexities including high-power consumption [7]. As shown in Figure 1, plasma actuators generate a plasma discharge on a wing surface, inducing a body force on the surrounding air. This causes the boundary layer air to accelerate, helping to maintain its attachment to the wing surface, thus delaying or preventing flow separation. As a result, plasma actuators can suppress flow separation, enhance the lift-drag ratio, and increase the maximum stall angle of a wing [8]. DBD plasma actuators offer several advantages over other types, such as plasma jets, including the absence of moving parts, simplicity, and control at high frequencies [9]. Successful implementation of DBD plasma actuators could mitigate the limitations of flight in laminar flow conditions and broaden the uses of fixed-wing aircraft.

For the purposes of this investigation, a NACA0012 airfoil was selected as a base for simulating the non-actuated and actuated flow around the wing due to its abundant use

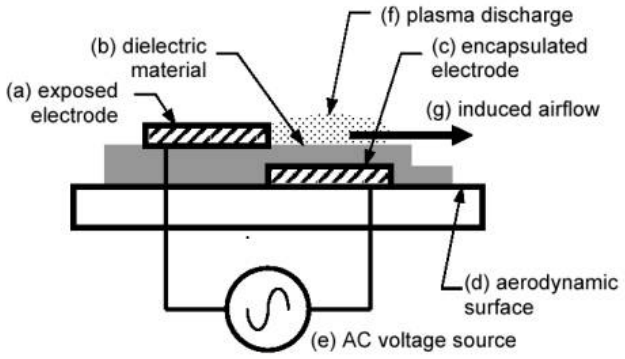

Figure 1: Schematic of a DBD plasma actuator [10].

in previous studies. Known for its well-documented stall behaviour and simple geometry, the NACA0012 airfoil is commonly used in aircraft and aerodynamic surface applications [11].

2 MATERIALS AND METHODS

To determine if a plasma actuator can cause delay in flow separation and increase the maximum lift coefficient, baseline stall angles without actuator influence are required for comparison. Stall angles are specific to airfoil geometry and R_e, therefore pre-existing studies on NACA0012 airfoils with R_e near the general range of MAVs (near 10,000 to 100,000) were investigated. Through experimentation and simulations, a study determined the stall angles of the NACA0012 near the desired R_e of 53,000 [12]. Thus, this R_e was selected for baseline simulations to record values for comparison to validate simulation parameters.

The range of simulated angles of attack, spanning from $4°$ to $16°$, correspond with those used in similar studies to determine if the implementation of actuators increased stall angle. The continual increase of the time-averaged lift coefficients past $10°$ - $11°$ would indicate that the plasma actuator effectively delayed flow separation, resulting in increased maximum lift [12]. Simulations are performed at a R_e of 53,000, and at increments of $0.5°$ determined to capture delayed flow separation without running redundant simulations.

The simulations aim to determine the optimal location of DBD plasma actuators on the wing by determining the locations of flow separation, thereby optimizing their effectiveness in preventing it. Simulations following this determination ran with the actuator placed at the identified location to evaluate its effectiveness.

Simscale was used with the goal of determining the angles of attack at which flow separation occured on the NACA0012, and the location along the chord length where there is boundary layer detachment. These simulations were also used to test appropriate airflow conditions, models, and meshes in the initial stages of the study, helping to inform their final iterations. However, the simulations produced results dissimilar to previous papers. The discrepancy is attributed to a lack of refinement in the mesh used in SimScale due to the limited resources available for this study. As a result, OpenFoam is used for subsequent simulations, where no limit on computational resources of the software is present.

The PIMPLE solver in PISO mode in OpenFOAM is used to perform a transient simulation with NACA0012 at a chord length of $0.10m$. An intensity of 0.15% is chosen to investigate laminar separation bubbles and to compare with previou sstudies. At the designated R_e, density of $1.0kg/m^3$ and kinematic viscosity of $1.50e-05m^2$/s, the angle of attack was varied by adjusting the x and y components of the free-stream velocity. A RAS simulation type with turbulence model $kw-sst$ is used.

The $k-\omega$ SST model was employed in this study due to its suitability for low R_e flows, combining the accuracy of $k-w$ modeling for near wall turbulence with the freestream stability of the k-e model for reduced sensitivity [13]. Three meshes are created and a grid convergence test is conducted. The chosen mesh averages $y+ < 3$ near the wall to ensure the viscous sub-layer is fully resolved.

Parameter	Mesh 1	Mesh 2	Mesh 3
Points	267408	309714	350816
Cells	132736	153750	174230
Max. Aspect Ratio	219.858	255.273	349.385
Max Non-Orthogonality	49.576	49.7978	50.8037
Max Skewness	0.719315	0.725961	0.674703
Average Lift Coefficient	0.796177	0.804454	0.812118
Average Drag Coefficient	0.078603	0.076696	0.066839

Table 1: Table detailing the parameters of the three constructed meshes.

The lift and drag coefficients of Mesh 1 and 2 shown in Table 1 has a difference of 1.03% and 2.43% respectively, whereas Mesh 2 and 3 have a difference of 0.95% and 12.85% for lift and drag coefficient respectively. The difference between Mesh 2 and 3 compared to Mesh 1 and 2 is attributed to the difference in max aspect ratio, max skewness, and max non-orthogonality. Due to the grid convergence results, Mesh 2 shown in Figure 2 was chosen to conduct the study.

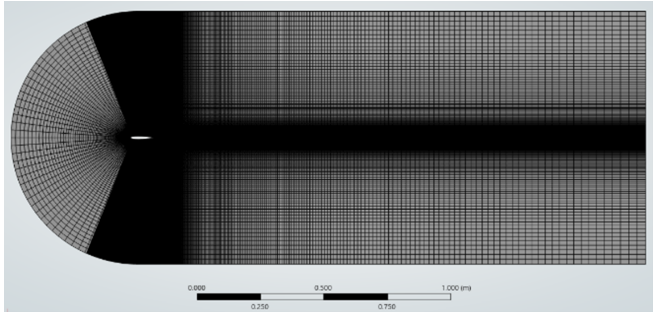

Figure 2: Mesh 2 in Ansys Meshing, with scale.

http://www.imavs.org/

The area around the airfoil shown in Figure 3 was further refined, however additional refinements of the mesh were not performed due to computational limitations caused by increasing file sizes and simulation run time from increasing vertical cell count.

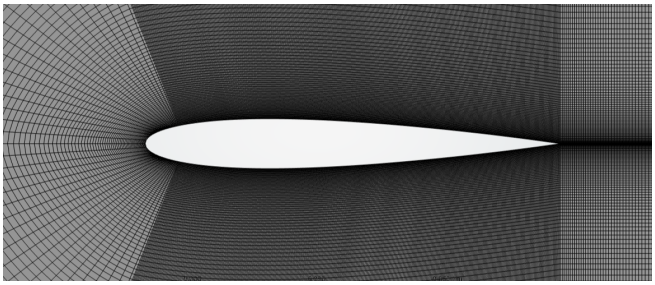

Figure 3: Mesh 2 near airfoil in Ansys Meshing.

The inlet for the boundary conditions has a fixed value condition while the topAndBottom and outlet uses inletOutlet. A no slip condition is applied to the airfoil. A two-second simulation without actuators at a maximum Courant number of one was conducted to validate boundary conditions. To implement the actuators, in the Navier-Stokes Equation 2, the momentum is applied as a body force F with dimensions in $\mathrm{m/s^2}$.

$$\frac{\partial \bar{u}}{\partial t} + \bar{u} \cdot \nabla \bar{u} = -\frac{1}{\rho}\nabla P + \nu \nabla^2 \bar{u} + F \tag{2}$$

Where $\bar{u}$ is the velocity vector in m/s, ρ is the density in kg/m^3, *P* is the pressure in Pa, ν is the kinematic viscosity in m^2/s, and *F* is the body force per unit mass in m/s^2.

To simulate the actuator, a rotatedBoxToCell cellset is created in topoSetDict to represent the plasma region on the airfoil and is positioned as discussed in Section 3. As demonstrated in the numerical study by Bernal Orozco et al. [13], using the Kloker model, the plasma region reaches up to $0.003m$ from the wall. Additionally, the force only extends significantly downstream the length of the embedded electrode. The region therefore has a length of $20mm$ and a height of $3mm$ [14]. The fvOptions utility is used to implement the plasma as a momentum source. The maximum body force is $416N/m^3$ as found by Hofkens [15] for a power source of $8kV$ and a frequency of $2kHz$. Maden et al [16] determined that the plasma distribution could be modeled as function of x and y coordinates. The model is calibrated to Hofkens' value [15] and integrated over the region to obtain the average force. The resulting integrated force density is determined to be $304.9N/m^3$.

The unsteadiness of the body force is then modeled using equation 3 [13].

$$f(x, y, t) = f(x, y)\sin^2(2\pi f t) \tag{3}$$

Using the vectorSemiImplicitSource option, a table with the time and its respective body force value is created for the duration of the simulation. The file is then read in the fvOptions and simulations are conducted with the actuators on and off.

All simulations write a .dat file containing the force coefficients and moments (lift, drag, pitching moment etc.). To simplify the processing of this data, a python script is written to output specific columns selected by the user in a csv file when a .dat file created by the simulation is given.

The meshes required for the study were created using Ansys meshing and exported as fluent .msh files where they were translated by OpenFOAM using the fluentMeshToFoam tool. All dimensions of the mesh were based on a single standard element size with all specific element sizes being a factor of the standard size. In the grid convergence, further refined meshes were made by reducing the standard element size to increase the total number of cells/elements by 10-15% per iteration.

To focus the refinement of the mesh around the airfoil a smooth transition bias is used with the growth rate along the height of the mesh being set to 1.04. This number is chosen as it is needed to keep the cells surrounding the airfoil edge in the wall function while optimizing the use of computational resources. The growth rate along the edge of the mesh behind the airfoil is set to 1.0175 to create a smooth gradient between the regions above and below the airfoil and the region behind the airfoil. The vertical bias used causes the cell aspect ratio to significantly increase for cells further vertically from the airfoil edge. However, due to limits in computational resources, further refinement of areas far from the airfoil edge vertically is not performed.

To improve simulations organization, a program is written using python that keeps track of simulation progress while redirecting the terminal output of the simulation into a file. The program reads the end time of the simulation from the controlDict file and converts it to a percentage displayed to the user along with an estimated completion time.

An assumption embedded into the OpenFOAM simulations is that the airfoil is perfectly smooth. This assumption differs from both experimental wind tunnel conditions and literature simulation values that employed the software XFoil. XFoil assumes low turbulence and relatively smooth surfaces [12]. In addition, the chord length in the Jardin et al. experiment is $0.15m$ whereas the following study is $0.10m$. Both factors are unlikely to have a significant impact on the results due to minimal differences, validated by the baseline lift coefficient values similarity to those in current studies.

To determine the location of flow separation at each simulated angle of attack, a Python script is written to process the results. The location of the separation point, identified by its distance along the chord of the airfoil from the leading edge, is approximated by searching for the point closest to the airfoil's leading edge with negative x-airflow velocity. The negative x-velocity signifies the presence of backflow, indicating appreciable separation of the boundary layer at that location.

http://www.imavs.org/

http://www.imavs.org/

This method did not determine exact separation points, but rather slightly further points where the boundary layer had fully separated, yielding an approximation of the true location.

The script can only process a single timestep of each simulation at a time, therefore the separation point for a given angle of attack is obtained from a single iteration of its simulation. Thus, the last iteration of each simulation is processed for this purpose. A visual analysis of several simulations indicates that this method is unlikely to produce significant error in the location of the separation points, as the leading side of the separation bubbles do not make significant position changes between timesteps.

3 TESTS AND RESULTS

Figure 4 displays the position of flow separation, as defined in Section 2, as a function of angle of attack for the actuated and non-actuated airfoil. The results are consistent with the established understanding that as the angle of attack increases, the flow separation point approaches the leading edge. The flow separation points for angles of attack greater than $4°$, for the non-actuated airfoil, are within $20mm$ of the airfoil's leading edge. Since the length of the actuator used is $20mm$, and DBD plasma actuators are most effective when positioned just before the separation point [17] , it is concluded that the optimal position of the actuator is with its front edge at the leading edge of the airfoil.

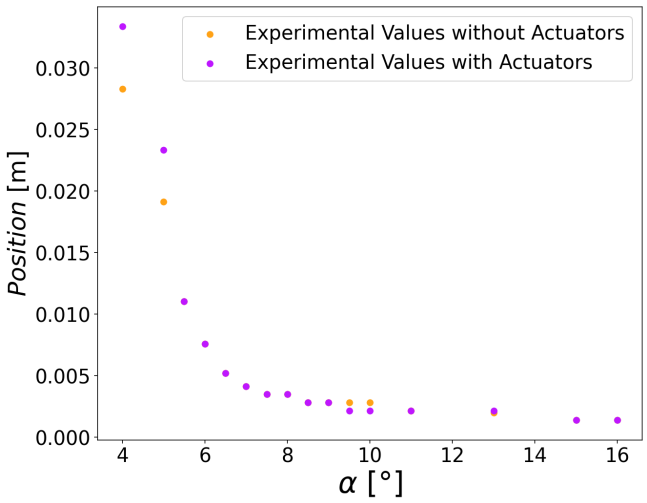

Figure 4: Graph of simulated position of flow separation vs angle of attack for actuated and non-actuated NACA0012 airfoil.

As shown in Figure 4, the majority of the positions of flow separation from the actuated simulations are at the same location as their corresponding non-actuated simulation, though some positions were further from the leading edge when actuated, such as $5°$ as shown in Figure 5. There are two exceptions, those being $9.5°$ and $10°$ which have flow separation closer to the leading edge when actuated. These exceptions are attributed to errors within the simulations, which may be amplified by the mesh refinement selected and discussed in Section 2.

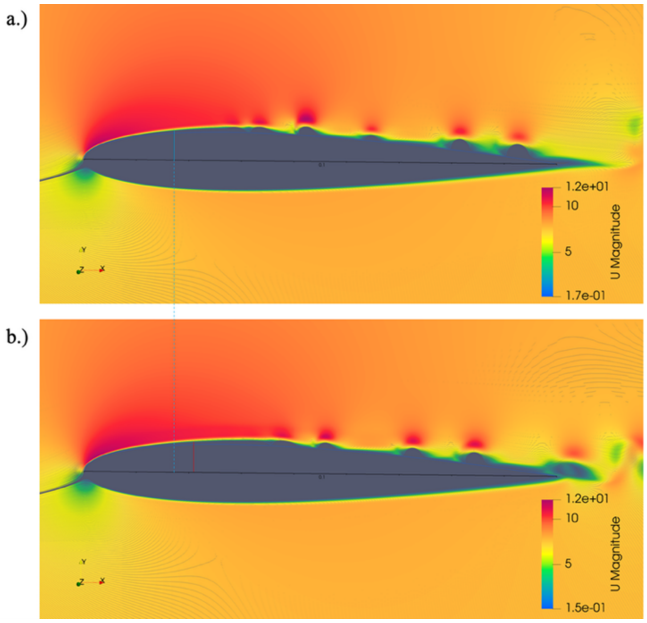

Figure 5: Airfoil at $5°$ angle of attack showing flow separation. Actuators delayed flow separation from 1.91 cm (a) to 2.33 cm (b).

Simulations with and without the actuator are conducted to validate its effectiveness at this position. Figure 6 compares the actuated and non-actuated lift values from these simulations to the non-actuated values found by Jardin et al [12].

The results demonstrate the actuator's effectiveness at increasing lift when placed at this location, as all simulated angles, with the exceptions of $9°$ and $15°$, yielded higher time - averaged lift coefficients when actuated. These exceptions are attributed to errors within the simulations.

Values from the Jardin study display that the stall angle for $R_e = 53,000$ is approximately $10°$. However, although the simulated data initially follows a similar trend, it does not display a stall angle within the experimental range. All results after $10°$ should therefore be interpreted cautiously. This overprediction can be attributed to a variety of reasons which Tank et Al [18] explored in depth. Notably, laminar separation and reattachment, unique to low R_e, is difficult to capture. Other research including Alleto's dynamic stall analysis [19] suggest that the Langtry-Menter $kw - sst$ model, also known as the $\gamma - \mathrm{R}_{e\theta}$ model, is more suitable for turbulence transition modeling. This should be explored in future works.

The lack of stall could also be attributed to the methodology. This study utilized time-averaged lift coefficients, which

http://www.imavs.org/

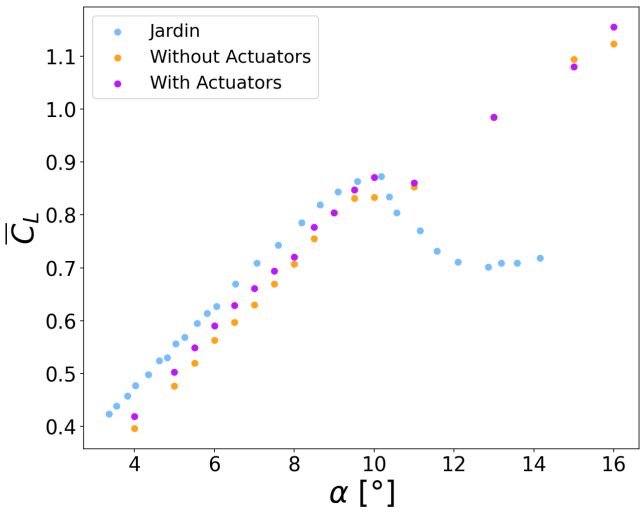

Figure 6: Graph of simulated lift coefficient vs angle of attack for non-actuated and actuated NACA0012 airfoil with comparison to Jardin literature values without actuators.

may not have fully captured transient stall conditions. At higher angles of attack around the anticipated stall angle of $10°$, the lift coefficient exhibited increased fluctuations compared to lower angles. These fluctuations increase until $16°$. Figure 7 shows the amplitude of these fluctuations at $5°$, $8.5°$, and $10°$ significantly increasing with angle of attack, indicative of stall behavior.

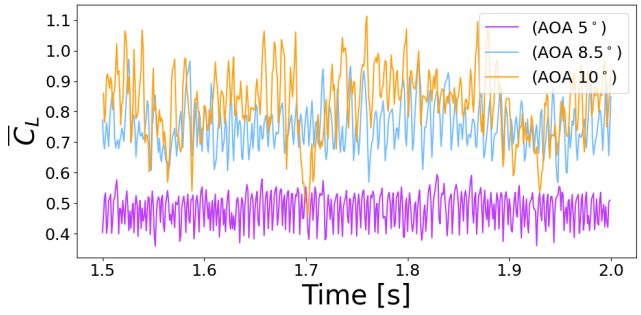

Figure 7: Lift coefficient from $1.5-2.0s$ for $5°$, $8.5°$, and $10°$ angle of attack with no actuators showing increasing fluctuations indicative of flow instability.

The sudden decrease in lift coefficient is attributed to laminar separation bubbles bursting [20], as shown in Figure 8. Despite these pronounced oscillations, the time-averaged lift coefficient continues to show an overall increasing trend.

Additionally, the $y+$ is greater than one due to limited computational resources. To ensure accuracy while fully resolving the viscous sub – layer, future works should further refine the mesh near the wall to $y+ < 1$.

Figure 9 displays the simulated coefficient of drag vs. angle of attack for the actuated and non-actuated simulations. The plot confirms the actuator's effectiveness at decreasing drag when placed at the airfoil's leading edge, as all simulated angles, with the exceptions of $11°$ and $13°$, yielded lower drag coefficients when actuated. These exceptions are attributed to errors within the simulations.

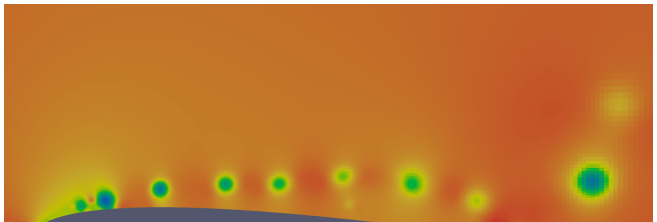

Figure 8: Laminar separation bubbles at $10°$ angle of attack with no actuator.

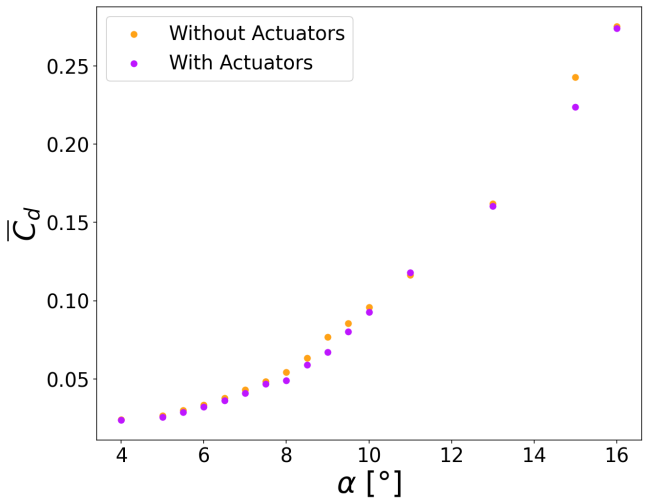

Figure 9: Graph of simulated drag coefficient vs angle of attack for non-actuated and actuated NACA0012 airfoil.

4 CONCLUSION

This study set out to find the optimal positions for DBD plasma actuators to mitigate flow separation and increase the stall angle for flight at low R_e. This technology has applications in improving flight performance in MAVs through expanding the range of conditions these vehicles can be expected to operate in.

The locations of flow separation for angles of attack past $5°$ are within the actuator length of $20mm$. Thus, the opti-

mal location of the actuator is directly at the leading edge of the airfoil. This location is validated by simulations with the actuator at this position. Most actuated simulations did not demonstrate an ability of the actuator to delay flow separation to further along the chord length. However, the actuated simulations display a trend of yielding higher lift and lower drag coefficients than the corresponding non-actuated simulations, demonstrating the effectiveness of the actuator at this location.

This study was not able to investigate the actuator's ability to increase the stall angle. Neither the actuated nor non-actuated simulations demonstrated a stall angle within the experimental range, which did not agree with data from previous studies used for comparison due the turbulence model used and the near-wall mesh refinement. Thus, the stall angle delay should be further explored in future studies.

Fabrication of a DBD plasma actuator for future investigation would include a thin electrode, possibly made of or containing graphene derivatives or electroplated silver. This would be placed on a dielectric material comprised of Kapton due to its low cost, flexibility, and high dielectric strength of 275.6 $V/\mu m$ at a thickness of 25.4 μm [21].

The actuator should implement a separate battery power source, as it is not ideal to interfere with the main MAV power. It can be built by using a MOSFET with a tailored threshold to control the frequency ($2kHz$), a transformer that can step up battery voltage into the ideal $8kV$ amplitude, a system (i.e. optocoupler) that can isolate the high voltage from the low, and resistors to ensure one meets the required voltage.

http://www.imavs.org/

ACKNOWLEDGMENTS

This work is part of the Queen's University Aerospace Design Team which received funding from the Smith Faculty of Engineering and Applied Sciences. The authors thank Sam Williamson, Dr. Francesco Ambrogi, Dr. Barbara L. da Silva, and Dr. John Kurelek for their contributions. This work was also supported by SimScale through their Academic Plan, which was used for preliminary simulations.

REFERENCES

[1] H. Sturm, G. Dumstorff, P. Busche, and D. Westermann. Boundary layer separation and reattachment detection on airfoils by thermal flow sensors. *Sensors*, 12(11):14292–14306, November 2012.

[2] J. Winslow, H. Otsuka, B. Govindarajan, and I. Chopra. Basic understanding of airfoil characteristics at low reynolds numbers (10–10). *Journal of Aircraft*, 55(3):1050–1061, 2018.

[3] R. Dumas, C. Renaud, and M. Villedieu. Numerical predictions of low reynolds number compressible aerodynamics. *Aerospace Science and Technology*, 85:211–223, 2019.

[4] N. Thipyopas and J.-M. Moschetta. A fixed-wing biplane mav for low speed missions. *International Journal of Micro Air Vehicles*, 1(1):13–24, 2009.

[5] S. Zhong, X. Wang, and Y. Liu. Control of laminar flow separation over a backward-facing rounded ramp with c-d riblets – the effects of riblet height, spacing and yaw angle. *International Journal of Heat and Fluid Flow*, 81:108629, 2020.

[6] A. Heidarian, H. Ghassemi, and P. Liu. Numerical analysis of the effects of riblets on drag reduction of a flat plate. *Journal of Applied Fluid Mechanics*, 11(3):679–688, 2018.

[7] F. Rodrigues, J. Páscoa, and F. Dias. Power consumption characterization of dbd plasma actuators for boundary layer control. In *International Conference on Engineering*, Covilhã, Portugal, 2015.

[8] R.-B. Liu, W.-T. Wei, H.-P. Wan, and J.-Y. Cheng. Experimental study on airfoil flow separation control via an air-supplement plasma synthetic jet. *Advances in Aerodynamics*, 4(1):35, 2022.

[9] L. Francioso, C. De Pascali, E. Pescini, M. G. De Giorgi, and P. Siciliano. Modeling, fabrication and plasma actuator coupling of flexible pressure sensors for flow separation detection and control in aeronautical applications. *Journal of Physics D: Applied Physics*, 49(23):235201, 2016.

[10] R. Pereira, G. J. W. van Bussel, and W. A. Timmer. Active stall control for large offshore horizontal axis wind turbines; a conceptual study. *Journal of Physics: Conference Series*, 555(1):012082, 2014.

[11] K. Asai, K. Nakano, and Y. Nonomura. Stalling characteristics of airfoils near the boundary between leading-edge stall and trailing-edge stall. *AIAA Journal*, 58(10):4291–4303, 2020.

[12] T. Jardin, V. Ferrand, and E. R. Gowree. Naca0012 airfoil at reynolds numbers between 50,000 and 140,000 — part 1: Steady freestream. *International Journal of Heat and Fluid Flow*, 112, 2025.

[13] R. A. Bernal Orozco, O. M. Huerta Chávez, J. Á. Ortega Herrera, and A. Arias Montaño. Numerical technique for implementation of sdbd plasma actuators. *Computación y Sistemas*, 26(4):1527–1538, 2022.

[14] M. B. S. Forte, F. Jolibois, M. P. Mignolet, E. Moreau, G. Artana, and G. Touchard. Optimization of a dielectric barrier discharge actuator by stationary and non-stationary measurements. *Experiments in Fluids*, 43(6):917–928, 2007.

[15] A. Hofkens. Determination of the body force generated by a plasma actuator through numerical optimization. Master's thesis, Delft University of Technology, 2016.

[16] I. Maden, A. Aksu, A. Topal, H. Yildiz, and E. Can Yilmaz. Experimental and computational study of the flow induced by a plasma actuator. *International Journal of Heat and Fluid Flow*, 41:80–89, 2013.

[17] T. C. Corke, P. O. Bowles, C. He, and E. H. Matlis. Sensing and control of flow separation using plasma actuators. *Philosophical Transactions of the Royal Society A*, 369(1940):1459–1475, 2011.

[18] J. Tank, L. Smith, and G. R. Spedding. On the possibility (or lack thereof) of agreement between experiment and computation of flows over wings at moderate reynolds number. *Interface Focus*, 7(1):20160076, 2017.

[19] M. Alletto. Dynamic stall naca0012. `https://wiki.openfoam.com/index.php?title=Dynamic_stall_NACA0012_Michael_Alletto&oldid=4388`, 2023. OpenFOAM Wiki.

[20] M. Ahmad N. Ali and R. R. Raja. Separation bubble characteristics over a naca 2415 airfoil at low reynolds number. *Journal of Physics: Conference Series*, 2054(1):012005, 2021.

[21] Jet Propulsion Laboratory. Material notes and tables. `https://descanso.jpl.nasa.gov/SciTechBook/series3/07Chapter6MatlNotesTables.pdf`, 2011. Chapter 6, SciTech Book Series III, Pasadena, CA.

http://www.imavs.org/